

PETROGRAPHIC SETTING OF BADDELEYITE IN ENRICHED BASALTIC SHERGOTTITES. A. I. Sheen¹ and C. D. K. Herd¹, ¹Department of Earth and Atmospheric Sciences, 1-26 Earth Sciences Building, University of Alberta, Edmonton, Alberta, Canada, T6G 2E3. (asheen@ualberta.ca).

Introduction and Background: Baddeleyite (ZrO₂) occurs as an accessory mineral in mafic igneous rocks and is widely analyzed in terrestrial U–Pb geochronology studies due to the mineral's ability to concentrate U while excluding Pb during crystallization, in addition to closed-system isotopic behavior during most modification processes, including shock [1, 2]. Application of U–Pb baddeleyite geochronology to Martian meteorites has been achieved by *in-situ* SIMS combined with high-resolution microstructural and chemical mapping which resolves igneous signatures from localized shock-induced isotopic disturbances [3, 4, 5]. Growing interest in *in-situ* isotopic analytical methods in light of planned sample return missions [e.g., 6, 7] highlights the need for more accessory-mineral based geochronology. A recent review [8] shows that baddeleyite crystallizes as part of the late-stage igneous assemblage and is more common at higher oxygen fugacity ($\geq 0 \log \Delta QFM$). Of the Martian meteorites examined by [8], baddeleyite is found to be most common in enriched basaltic shergottites.

To arrive at a more comprehensive understanding of baddeleyite occurrences in enriched basaltic shergottites, we conduct a petrographic survey of new specimens, including those recently described. Textural and compositional characterization of associated mineral assemblages are combined to elucidate controls on baddeleyite occurrence, its morphology, and size. The goal of the study seeks to identify suitable targets for U–Pb baddeleyite geochronology.

Approach: Eight enriched basaltic shergottites were selected for analysis: Jiddat al Harasis (JaH) 479, Ksar Ghilane (KG) 002, Northwest Africa (NWA) 10299, 11057, 11073, 11255, 12262, and 12919. EPMA analyses were conducted on a Cameca SX100 at the Department of Earth and Atmospheric Sciences, University of Alberta. A representative area of each

polished thin section or tile was mapped for Na, Mg, Si, P, Cl, Ca, Ti, Fe, and Zr at resolutions between 4 and 7 $\mu\text{m}/\text{pixel}$. The Zr element maps were utilized to locate baddeleyite grains of sufficient size (generally $>1 \mu\text{m}$); each occurrence was further documented using BSE imaging.

Mineral compositions were determined for phases associated with baddeleyite, including pyroxene, maskelynite, Fe–Ti oxides and, where applicable, late-stage olivine and olivine-pyroxene-silica symplectite. Whole-rock powders of NWA 10299, 11057, 12262, and 12919 were analyzed for bulk trace elements by ICP-MS at the Department of Earth and Atmospheric Sciences, University of Alberta.

Results: A summary of the baddeleyite search and characterization is reported in Table 1. The frequency of identifiable grains ranges between 0.6 and 1.1 grains/ mm^2 for six samples, while two samples (NWA 12262 and NWA 12919) contain more abundant baddeleyites, at 2.2–2.5 grains/ mm^2 . Average grain dimensions range between 2.5 and 6.7 μm , while the largest grain in each sample ranges between 7 and 24 μm in the longest dimension. Average aspect ratios range between 2.1 and 3.3.

Baddeleyite occurrences are generally divided into three categories (in decreasing frequency): 1) as part of late-stage assemblages containing Fe–Ti oxides, Fe-sulfides, Ca-phosphates, fayalitic olivine, and/or pigeonitic pyroxene (Fig. 1), 2) in pockets of silica+K-feldspar mesostasis, and 3) as isolated inclusions within pigeonitic pyroxene or maskelynite. Baddeleyite grains in the first category generally reach the largest sizes, especially when associated with Fe–Ti oxides in which case they tend to be more often euhedral (Fig. 1b). In a few samples, very fine ($<1 \mu\text{m}$) baddeleyite rims the edge of silica inclusions within titanomagnetite and olivine.

Table 1. Baddeleyite frequency and grain dimension statistics determined through EPMA mapping.

Sample	Frequency (n/ mm^2)	Avg. Grain Length (μm)	σ	Max. Grain Length (μm)	Avg. l:w Ratio	n	Pyx. Fs Endmember (%)*	Oxygen Fugacity ($\log \Delta QFM$)	σ	La/Yb _(N) **
JaH 479	0.9	6.7	1.5	24	2.8	97	21-83	-1.2	0.3	0.75
KG 002	0.6	3.7	2.3	8	2.6	24	26-82	-1.0	0.2	0.85
NWA 10299	1.1	5.0	2.8	10	2.4	76	22-69	-1.4	0.5	0.94
NWA 11057	0.8	3.3	3.2	7	2.3	36	22-60	-1.4	0.2	0.87
NWA 11073	0.8	2.7	1.9	9	2.4	30	24-61	-1.5	0.2	0.88
NWA 11255	0.8	3.0	2.1	8	2.6	34	22-59	-1.1	0.1	0.93
NWA 12262	2.2	3.2	2.3	10	2.1	79	24-83	+0.1	0.1	1.03
NWA 12919	2.5	2.5	2.4	14	3.3	106	19-68	-1.1	0.2	0.87

* Pyroxene data sources: KG 002 [9], NWA 12262 [10]; remaining values are from this study. ** Bulk rock, normalized to CI values. Data sources: JaH 479 [11], KG 002 [9], NWA 11073 and 11255 [12].

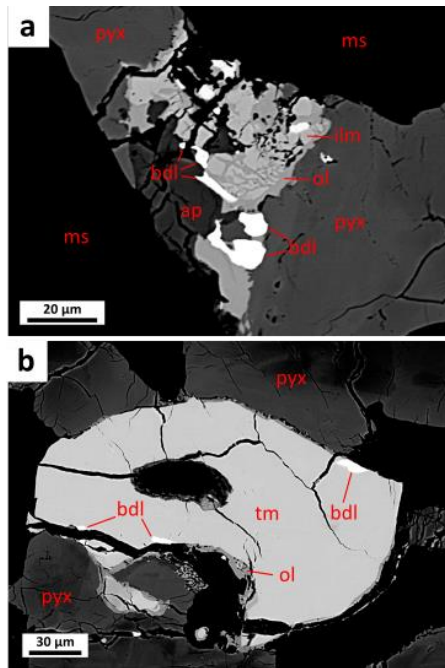


Fig 1. BSE images of baddeleyites in late-stage assemblages in a) NWA 12919 and b) NWA 10299. Pyx: pyroxene, tm: titanomagnetite, ilm: ilmenite, ol: olivine, bdl: baddeleyite, ap: apatite, ms: maskelynite.

Baddeleyite occurrences are summarized as follows:

JaH 479. Mostly anhedral, adjacent to coarse mesostasis, or at the boundary between three-phase symplectite and maskelynite.

KG 002. Mostly anhedral to subhedral, adjacent to or enclosed within titanomagnetite, Fe-sulfide, or fayalitic olivine.

NWA 10299. Mostly singular, prismatic to subhedral inclusions within titanomagnetite, and less commonly adjacent to other mesostasis minerals. Very small grains (<1 μm) are scattered within silica+K-feldspar mesostasis.

NWA 11057, 11073, and 11255. Most commonly in mesostasis at the pyroxene-maskelynite boundary. Largest grains tend to occur adjacent to Fe-Ti oxides. Where ilmenite is present alongside titanomagnetite, baddeleyite is nearly always adjacent to ilmenite. Much finer baddeleyite (<3 μm) is found within silica+K-feldspar mesostasis.

NWA 12266. Mostly in mesostasis pockets of pigeonitic pyroxene, fayalitic olivine, silica, Ca-phosphates, Fe-sulfides, and/or Fe-Ti oxides. The largest grains tend to occur at the boundary between pyroxene and silica+K-feldspar mesostasis.

NWA 12919. Larger grains (>5 μm) are commonly adjacent to Fe-Ti oxides in mesostasis. Titanomagnetite grains along the edge of silica+K-feldspar mesostasis contain smaller (<2 μm) baddeleyite grains.

Implications and Future Work: The prevalence of baddeleyite occurring in mesostasis alongside Fe-Ti oxides, Ca-phosphates, and Fe-sulfides indicates crystallization from late-stage melts enriched in incompatible elements such as Ti, P, K, S, and Zr. Baddeleyite crystallization therefore depends on the degree of melt fractionation. Pyroxene compositions of NWA 11057, 11073, and 11255 have a narrower ferrosilite endmember range (22–61%) compared to the other five shergottites (19–83%) and suggest less extensive fractional crystallization, consistent with the lower frequency of baddeleyite in these samples. Although KG 002 also has a large pyroxene ferrosilite endmember range, its much coarser grain size may have caused pyroxene and Fe-Ti oxides to become the major Zr sinks, limiting baddeleyite crystallization in mesostasis.

It has been proposed that oxygen fugacity imparts control on baddeleyite crystallization via incompatibility of Zr in Fe-Ti oxides [8]. Oxygen fugacity of seven out of eight studied shergottites shares a similar range of -1.5 to -1.1 logΔQFM, with NWA 12262 being more oxidized, at +0.1 logΔQFM. However baddeleyite frequency in NWA 12262 (2.2 grains/mm²) is similar to that in NWA 12919 (2.5 grains/mm²). Other first-order controls such as bulk Zr content need to be assessed in order to determine the effect of oxygen fugacity on baddeleyite crystallization among the studied shergottites.

Our findings thus far demonstrate that baddeleyite is common in enriched basaltic shergottites and that some grains are of sufficient size for SIMS U-Pb geochronology. Assessment of feasibility for SIMS U-Pb baddeleyite geochronology of the studied shergottite suite is ongoing.

Acknowledgments: Samples for this study are provided by Tony Irving (NWA 11057, 11073, 11255, 12266) and Julia Roszjar (KG 002). Analytical assistance was provided by Andrew Locock (EPMA) and Guangcheng Chen (ICP-MS). Funding by NSERC Grant RGPIN-2018-04902 to CDKH and NSERC CGS-D to AIS.

References: [1] Heaman L.M. and LeCheminant A.N. (1993) *Chem. Geol.*, 110, 95-126. [2] Niihara T. et al. (2012) *EPSL*, 341, 195-210. [3] Moser D.E. et al. (2013) *Nature*, 499, 454-458. [4] Zhou Q. et al. (2013) *EPSL*, 374, 156-163. [5] Darling J.R. et al. (2016) *EPSL*, 444, 1-12. [6] Bellucci J.J. et al. (2016) *EPSL*, 433, 241-248. [7] Bellucci J.J. et al. (2018) *EPSL*, 485, 79-87. [8] Herd C.D. et al. (2018) *AGU Monograph*, 137-166. [9] Llorca J. et al. (2013) *Meteorit. Planet. Sci.*, 48, 493-513. [10] Jean M.M. et al. (2016) *LPS XLVII*, Abstract #2698. [11] Lorenz C.A. et al. (2010) *Meteorit. Planet. Sci.*, 45, A121. [12] Lapen T.J. et al. (2018) *LPS XLIX*, Abstract #2773.